Magnetic Resonance in Medicine 67:1673–1683 (2012)

The Central Signal Singularity Phenomenon in Balanced SSFP and Its Application to Positive-Contrast Imaging

R. Reeve Ingle,[1]* Tolga Çukur,[2] and Dwight G. Nishimura[1]

Small perturbations of steady-state sequence parameters can induce very large spectral profile deviations that are localized to specific off-resonant frequencies, denoted critical frequencies. Although, a small number of studies have previously considered the use of these highly specific modulations for MR angiography and elastography, many potential applications still remain to be explored. An analysis of this phenomenon using a linear systems technique and a geometric magnetization trajectory technique shows that the critical frequencies correspond to singularities in the steady-state signal equation. An interleaved acquisition combined with a complex difference technique yields a spectral profile containing sharp peaks interleaved with wide stopbands, while a complex sum technique yields a spectral profile similar to that of balanced steady-state free precession. Simulations and phantom experiments are used to demonstrate a novel application of this technique for positive-contrast imaging of superparamagnetic iron-oxide nanoparticles. The technique is shown to yield images with high levels of positive contrast and good water and fat background suppression. The technique can also simultaneously yield images with contrast similar to balanced steady-state free precession. Magn Reson Med 67:1673–1683, 2012. © 2011 Wiley Periodicals, Inc.

Key words: balanced SSFP; oscillating steady states; positive contrast; SPIO; pulse sequence

The balanced steady-state free precession (bSSFP) sequence (1,2) has a periodic spectral profile that varies with off-resonant frequency. Many modifications to the bSSFP sequence have been developed to alter the spectral profile, including methods to diminish the variation with off-resonant frequency (e.g., to reduce the so-called banding artifact) (3–5) and methods to enhance the variation with off-resonant frequency (e.g., to suppress the fat signal) (6–16). When modifying the bSSFP sequence or when designing multiple repetition time (TR) sequences, certain configurations of excitations and TRs result in localized spikes or dips in the spectral profile. These spectral profile deviations are often found in profiles generated by automatic design techniques (8) as well as certain oscillating and multi-TR sequences (11–14,17). The phenomenon has previously been denoted central signal dip (13), and methods for preventing the occurrence of central signal dip in a multi-TR design technique have been proposed (16). In this work, we refer to this phenomenon as the central signal singularity phenomenon, and we show that spectral dips as well as spikes and other spectral profile deviations can be induced by perturbations to the bSSFP sequence.

Specific phase-perturbed SSFP sequences have been studied using geometric and linearization techniques (12,17). To our knowledge, however, no thorough analysis of the central signal singularity phenomenon, including the cause of the localized spectral profile deviations, has previously been conducted. A better understanding of this phenomenon will be useful for steady-state sequence design, enabling the prevention of these sharp spikes and dips, which can lead to unwanted signal modulation and banding artifacts. Furthermore, knowledge of how different factors affect the width, depth, and location of the spectral spikes and dips will be useful for designing novel pulse sequences that utilize the central signal singularity phenomenon.

In this work, we explore the central signal singularity phenomenon and provide an analysis of its causes via algebraic and geometric techniques. We illustrate the phenomenon using Bloch simulations of flip-angle-perturbed, RF phase-perturbed, and TR-perturbed bSSFP sequences, and we show that small, alternating perturbations of flip angles (α), RF phases (ϕ), or TRs cause sharp, localized deviations in the spectral profile. We analyze an α-perturbed SSFP sequence using an eigendecomposition technique as well as a geometric magnetization trajectory approach. These techniques can be easily generalized to analyze the central signal singularity phenomenon in other steady-state sequences, such as ϕ-perturbed SSFP, TR-perturbed SSFP, and multi-TR SSFP sequences.

After presenting a detailed explanation of the theory of the central signal singularity phenomenon, we demonstrate an application of the phenomenon to positive-contrast imaging, whereby field perturbations near iron-containing contrast agents, such as superparamagnetic iron-oxide (SPIO) nanoparticles, yield hyperintense signal (18–22). We introduce three perturbed differenced SSFP (pdSSFP) sequences: α-pdSSFP, ϕ-pdSSFP, and TR-pdSSFP. We use Bloch simulations, scans of a homogeneous phantom for spectral profile measurement, and scans of an agar gel phantom containing SPIO nanoparticles to assess the performance of the pdSSFP sequences for positive-contrast imaging. The pdSSFP sequences achieve good water and fat background suppression and generate positive contrast surrounding regions containing SPIO nanoparticles. The pdSSFP sequences use an interleaved acquisition strategy during odd and even TRs and are able to simultaneously

[1]Magnetic Resonance Systems Research Laboratory, Department of Electrical Engineering, Stanford University, Stanford, California, USA
[2]Helen Wills Neuroscience Institute, University of California, Berkeley, California, USA

Grant sponsor: National Science Foundation (NSF) Graduate Research Fellowship; Grant number: DGE-0645962; Grant sponsor: National Defense Science and Engineering Graduate (NDSEG) Fellowship; Grant number: 32 CFR 168a; Grant sponsor: National Institutes of Health; Grant number: R01 HL097516 and R01 HL075803; Grant sponsors: Stanford Graduate Fellowship, GE Healthcare.

*Correspondence to: Reeve Ingle, Packard Electrical Engineering Bldg, Room 210, 350 Serra Mall, Stanford, CA 94305-9510. E-mail: ringle@stanford.edu

Received 9 June 2011; revised 20 July 2011; accepted 26 July 2011.
DOI 10.1002/mrm.23156
Published online 24 October 2011 in Wiley Online Library (wileyonlinelibrary.com).

generate positive-contrast images (via a complex difference technique) and images with contrast similar to bSSFP (via a complex sum technique). Due to the interleaved acquisition technique, these images are inherently coregistered.

THEORY

The bSSFP pulse sequence is a periodic pulse sequence that consists of a single excitation per period and excitation and imaging gradients that are fully refocused over each period. TR is typically much shorter than T_1 and T_2 such that the resulting steady-state magnetization contains a large transverse component. Nominally, all excitations have the same flip angle, and the phase cycling scheme is usually chosen such that the RF phases alternate between 0° and 180° for consecutive excitations. The bSSFP spectral profile is periodic with period 1/TR, and it has smooth, continuous passband regions flanked by sharp, rapidly-varying transition-band regions.

Perturbed SSFP

Small, alternating perturbations of parameters in a bSSFP sequence can cause large, highly localized deviations in the magnetization profile. These deviations occur at specific frequencies in the center of the passband and can result from perturbations in the flip angle, RF phase, or TR. Three different perturbed SSFP sequence diagrams are shown in Fig. 1. Figure 1a shows an α-perturbed sequence, where the flip angles of odd and even excitations have been perturbed by $-\Delta\alpha/2°$ and $\Delta\alpha/2°$, respectively. Figure 1b shows a ϕ-perturbed sequence, where the RF phases of even excitations have been perturbed by $\Delta\phi$ degrees. Figure 1c shows a TR-perturbed sequence, where the odd and even TRs have been perturbed by $-\Delta TR/2$ ms and $\Delta TR/2$ ms, respectively. The spectral profiles in even and odd TRs are shown in Fig. 2, where the following parameters were used: TR = 4.6 ms (α- and ϕ-perturbed), TR = 6.9 ms (TR-perturbed), $\alpha = 60°$, $\Delta\alpha = 1°$, $\Delta\phi = 5°$, $\Delta TR = 0.1$ ms, $T_1/T_2 = 1000/200$ ms. These parameters were chosen to illustrate the different features of the perturbed SSFP sequences. The perturbations yield alternating even- and odd-TR steady-state magnetization profiles that have large deviations from the bSSFP profile in the center of the passband but little change in the transition-band. The deviations are localized to a small set of distinct frequencies that we denote critical frequencies.

In the following two sections, we present two corresponding analyses of the perturbed SSFP sequences, focusing on the spectral profile deviations that occur at the critical frequencies. In the first section, we use a linear systems approach in which the matrix expression for the steady-state magnetization is analyzed via eigendecomposition (23,24). In the second section, we use a geometric approach in which the trajectory of the steady-state magnetization vector is plotted for different off-resonant frequencies (25).

Linear Systems Analysis

A steady-state sequence can be represented by a fundamental period that is repeated to form the entire sequence. For

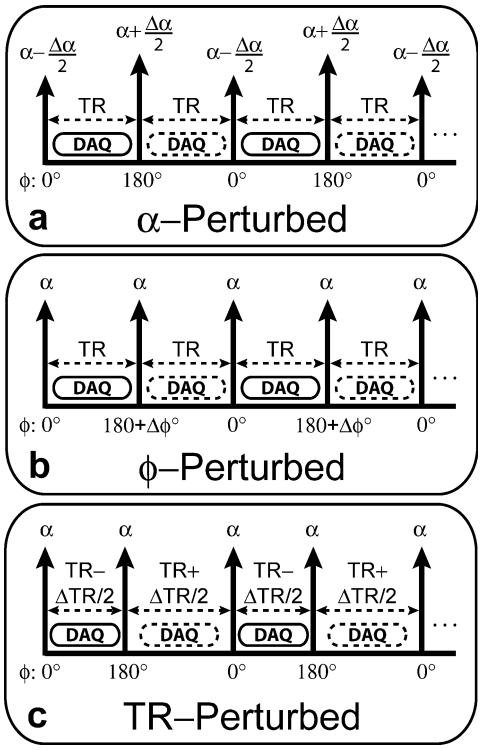

FIG. 1. The pulse sequence diagrams for the **(a)** flip-angle-perturbed SSFP, **(b)** phase-perturbed SSFP, and **(c)** TR-perturbed SSFP sequences.

the case of a perturbed SSFP sequence, the fundamental period consists of an even and odd TR. The magnetization change over one period is

$$\mathbf{M}_{k+1} = \mathbf{R}\mathbf{M}_k + \mathbf{b}, \quad [1]$$

where $\mathbf{M}_k$ and $\mathbf{M}_{k+1}$ are the magnetization (M_x, M_y, M_z) at the beginning and end of the period, $\mathbf{R}$ is a 3×3 matrix accounting for excitation, precession, and relaxation during the period, and $\mathbf{b}$ is a 3×1 vector that is a function of excitation, precession, and relaxation during even and odd TRs. In steady state, $\mathbf{M}_k = \mathbf{M}_{k+1} = \mathbf{M}_{ss}$, and Eq. 1 can be solved for the steady-state magnetization ($\mathbf{M}_{ss}$), yielding

$$\mathbf{M}_{ss} = (\mathbf{I} - \mathbf{R})^{-1}\mathbf{b}. \quad [2]$$

Equation 2 is a complicated function of the sequence parameters, with the matrix $\mathbf{R}$ and the vector $\mathbf{b}$ being composed of numerous products of rotation matrices and diagonal relaxation matrices. For example, the matrix $\mathbf{R}$ for the α-perturbed SSFP sequence is

$$\mathbf{R} = \mathbf{R}_x(\alpha - \Delta\alpha/2) \times \mathbf{E}\,\mathbf{R}_z(2\pi f\,\mathrm{TR})\,\mathbf{R}_{-x}(\alpha + \Delta\alpha/2)\,\mathbf{E}\,\mathbf{R}_z(2\pi f\,\mathrm{TR}), \quad [3]$$

and the vector $\mathbf{b}$ is

$$\mathbf{b} = \mathbf{R}_x(\alpha - \Delta\alpha/2) \times [\mathbf{E}\,\mathbf{R}_z(2\pi f\,\mathrm{TR})\,\mathbf{R}_{-x}(\alpha + \Delta\alpha/2) + \mathbf{I}](\mathbf{I} - \mathbf{E})\mathbf{M_0}, \quad [4]$$

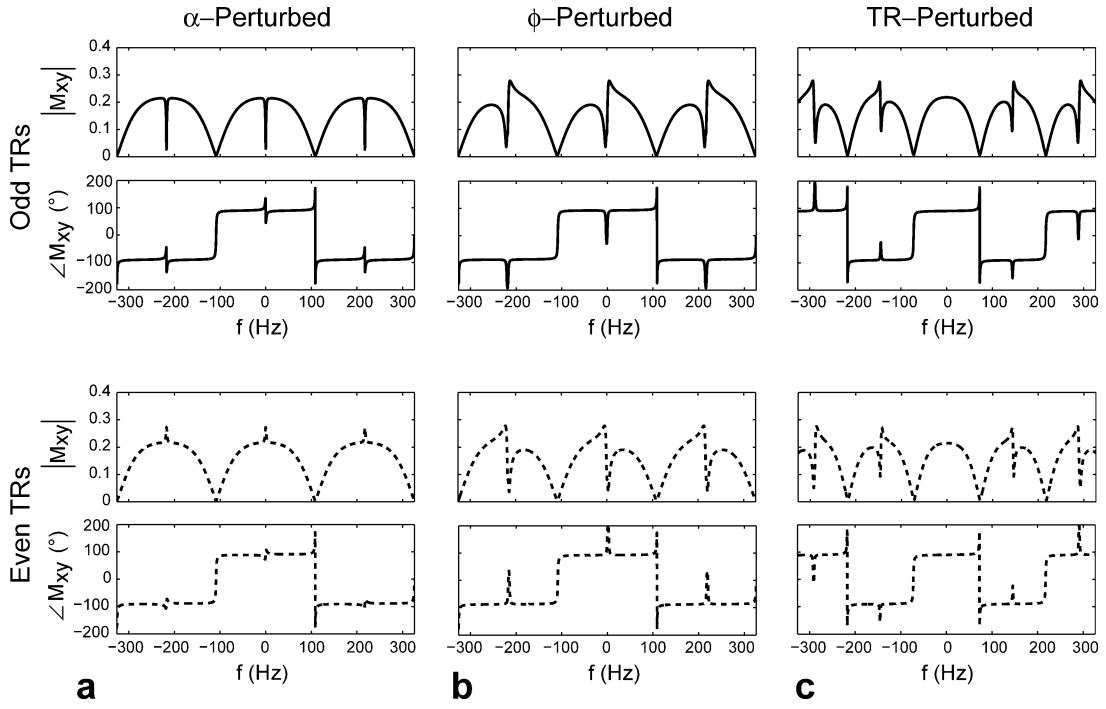

FIG. 2. The spectral profiles in even and odd TRs for the **(a)** flip-angle-perturbed SSFP, **(b)** phase-perturbed SSFP, and **(c)** TR-perturbed SSFP sequences. The profiles were simulated using $\alpha = 60°$ and $T_1/T_2 = 1000/200$ ms. a: Flip-angle perturbation $\Delta\alpha = 1°$ and TR = 4.6 ms were simulated. The alternating $\pm\Delta\alpha/2°$ perturbations of flip angles yield sharp, localized dips and spikes in the center of the magnitude profile during odd and even TRs, respectively. b: Phase perturbation $\Delta\phi = 5°$ and TR = 4.6 ms were simulated. The $\Delta\phi°$ phase perturbations of even excitations induce discontinuities in the center of the magnitude profile during odd and even TRs. c: TR perturbation ΔTR = 0.1 ms and TR = 6.9 ms were simulated. The alternating $\pm\Delta$TR/2-ms perturbations of TRs yield spectral profile discontinuities that vary in magnitude with off-resonant frequency. The phase profiles of all three sequences contain similar perturbations located at the same frequencies. The additional 180° phase due to the (0, 180)° phase schedule has been removed from the even-TR phase profiles.

where $\mathbf{R}_{\pm x}(\theta)$ represents a clockwise rotation of θ about the $\pm x$-axis, $\mathbf{R}_z(\theta)$ represents a clockwise rotation of θ about the z-axis, $\mathbf{E} = \text{diag}[e^{-\text{TR}/T_2}, e^{-\text{TR}/T_2}, e^{-\text{TR}/T_1}]$, $\mathbf{M_0}$ is the equilibrium magnetization, and f is the off-resonant frequency in Hz. The analysis can be greatly simplified by computing the eigendecomposition of $\mathbf{R}$,

$$\mathbf{R} = \mathbf{V}\mathbf{\Lambda}\mathbf{V}^{-1}, \qquad [5]$$

where $\mathbf{V}$ is a 3×3 matrix whose columns ($\mathbf{v}_1$, $\mathbf{v}_2$, and $\mathbf{v}_3$) are the eigenvectors of $\mathbf{R}$, and $\mathbf{\Lambda}$ is a 3×3 diagonal matrix whose diagonal entries (λ_1, λ_2, and λ_3) are the eigenvalues of $\mathbf{R}$. Substituting Eq. 5 into Eq. 2, the steady-state magnetization can be expressed as

$$\mathbf{M}_{\text{ss}} = \mathbf{V}(\mathbf{I} - \mathbf{\Lambda})^{-1}\mathbf{V}^{-1}\mathbf{b}. \qquad [6]$$

Equation 6 can be interpreted as follows. First, the vector $\mathbf{b}$ is decomposed into its components along each eigenvector. Then, each of these components is scaled independently by $(1 - \lambda_i)^{-1}$, which are the three components of the diagonal matrix $(\mathbf{I} - \mathbf{\Lambda})^{-1}$. Finally, the multiplication by $\mathbf{V}$ transforms the result back into the Cartesian coordinate system (24). There are two notable special cases that should be considered when analyzing Eq. 6. The first is when one eigenvalue is much closer to 1 than the other two, which occurs at most off-resonant frequencies. The second is when all three eigenvalues are close to 1, which occurs at the critical frequencies.

When one eigenvalue (say, λ_1) is much closer to 1 than the other two, $|(1 - \lambda_1)^{-1}|$ is much larger than the magnitude of the other two components of the diagonal matrix $(\mathbf{I} - \mathbf{\Lambda})^{-1}$. Subsequently, $\mathbf{M}_{\text{ss}}$ is directed nearly parallel to $\mathbf{v}_1$. In this case, knowledge of the dominant eigenvector, $\mathbf{v}_1$, is sufficient to determine the direction of the steady-state magnetization vector. Since $\mathbf{R}$ is composed of a product of rotation matrices (each having one eigenvalue equal to one) and a small amount of exponential damping ($\mathbf{E} \approx \mathbf{I}$), at most off-resonant frequencies, $\mathbf{R}$ has one real eigenvalue that is close to 1, and the other two eigenvalues form a complex conjugate pair that is much farther from 1. Thus, at these off-resonant frequencies, $\mathbf{M}_{\text{ss}}$ smoothly "tracks" the corresponding real eigenvector, which yields a smooth and continuous spectral profile. This phenomenon is demonstrated in Fig. 3 for a standard bSSFP sequence. Figure 3a plots the eigenvalues of $\mathbf{R}$ for an off-resonant frequency of 60 Hz, showing one dominant eigenvalue that is close to 1. Figure 3b shows the corresponding dominant eigenvector ($\mathbf{v}_1$) and the steady-state magnetization vector, which are coaligned.

The second notable special case occurs when all three eigenvalues of $\mathbf{R}$ are close to 1, or equivalently, $\mathbf{R} \approx \mathbf{I}$. This condition yields a singularity in the steady-state signal

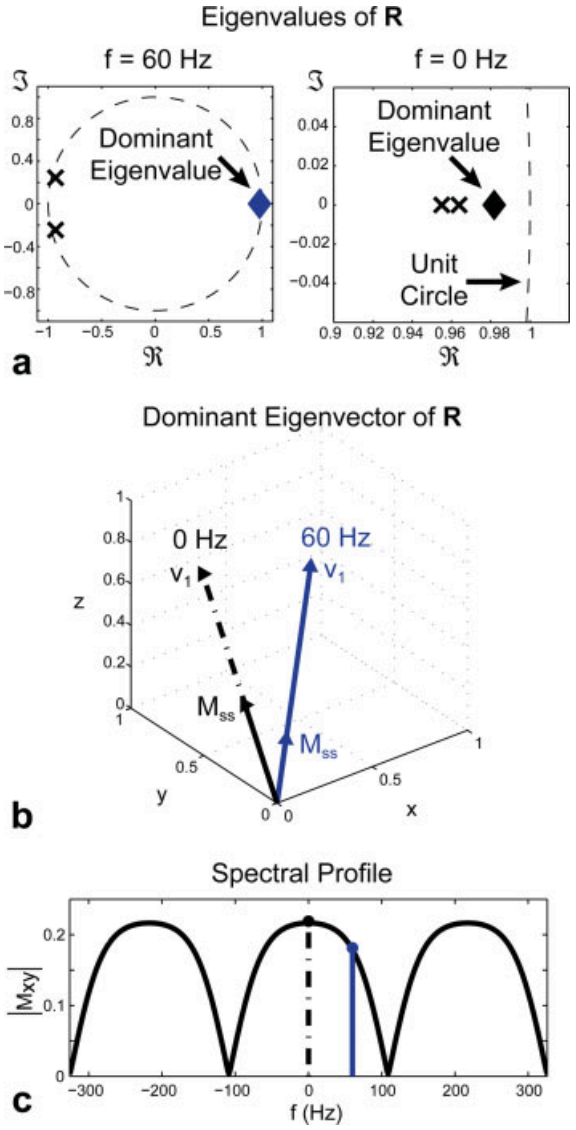

FIG. 3. The eigenvalues **(a)** and eigenvectors **(b)** of the system matrix **R** of a bSSFP sequence are plotted for two different off-resonant frequencies shown on the spectral profile **(c)**. a: At $f = 60$ Hz, there is one dominant, real eigenvalue that is close to 1 (blue diamond) and two complex eigenvalues that are far from 1. At $f = 0$ Hz, all three eigenvalues are real and close to 1, but one eigenvalue (black diamond) remains closest to 1. b: At both frequencies, the steady-state magnetization is parallel to the corresponding dominant eigenvector $\mathbf{v_1}$. c: The spectral profile is smooth and continuous since the steady-state magnetization vector tracks $\mathbf{v_1}$ across all frequencies. [Color figure can be viewed in the online issue, which is available at wileyonlinelibrary.com.]

equation (Eqs. 2 and 6). At these off-resonant frequencies, small changes of the steady-state sequence parameters yield small changes of **R**, which in turn are magnified into very large changes of $\mathbf{M}_{ss}$, since $\|(\mathbf{I} - \mathbf{R})^{-1}\|$ is very large. Thus, these off-resonant frequencies are the critical frequencies mentioned previously.

For the case of bSSFP, the critical frequencies occur at integer multiples of 1/TR Hz, located in the center of the passband of the spectral profile. In the absence of sequence perturbations (i.e., $\Delta\alpha = \Delta\phi = \Delta\mathrm{TR} = 0$), all three eigenvalues of **R** are real (since **R** is symmetric) and close to 1 at $f = 0$ Hz, but there is still one dominant real eigenvalue that is closer to 1 than the other two (Fig. 3a). Although the magnitudes of the three eigenvalues are very similar, the inversion via $(\mathbf{I} - \mathbf{\Lambda})^{-1}$ amplifies the relatively small differences between the eigenvalues, yielding a dominant eigenvector corresponding to the eigenvalue that is closest to one. The steady-state magnetization continues to "track" the dominant eigenvector through these critical frequencies (Fig. 3b), resulting in a smooth spectral profile having no sharp deviations at these frequencies (Fig. 3c). In the presence of sequence perturbations, however, **R** has a complex pair of dominant eigenvalues at the critical frequencies, and $\mathbf{M}_{ss}$ no longer tracks a single eigenvector. Consequently, the direction of $\mathbf{M}_{ss}$ changes significantly, resulting in large deviations in the spectral profile. Figure 4a plots the eigenvalues of **R** for an α-perturbed SSFP sequence with $\Delta\alpha = 1°$, at $f = 0$ Hz. At this critical frequency, the two complex eigenvalues of **R** are closest to 1, and the steady-state magnetization lies

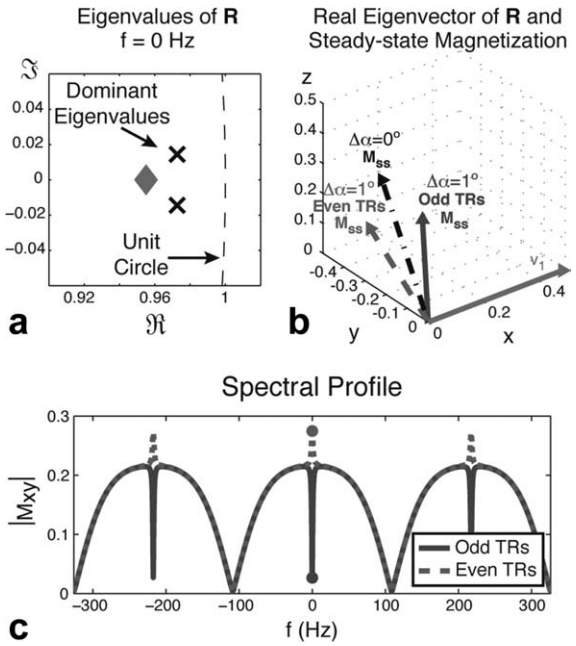

FIG. 4. The eigenvalues **(a)** and eigenvectors **(b)** of the system matrix **R** of an α-perturbed SSFP sequence are plotted for $f = 0$ Hz. a: The pair of complex eigenvalues is dominant, and the real eigenvalue (red diamond) is farther from 1. b: The steady-state magnetization vectors during even and odd TRs are linear combinations of the corresponding complex eigenvectors, which are orthogonal to the real eigenvector $\mathbf{v_1}$. Both the complex eigenvalues and the complex eigenvectors occur in complex conjugate pairs, and the linear combination results in a steady-state magnetization vector with real components, positioned in the *y*-*z* plane, orthogonal to $\mathbf{v_1}$. $\mathbf{M}_{ss}$ is oriented more longitudinally during odd TRs and closer to the transverse plane during even TRs, compared to $\mathbf{M}_{ss}$ of a bSSFP sequence (dotted black). c: Since the steady-state magnetization vector does not track $\mathbf{v_1}$ at $f = 0$ Hz (and other critical frequencies), sharp dips and spikes are induced in the odd and even spectral profiles, respectively. [Color figure can be viewed in the online issue, which is available at wileyonlinelibrary.com.]

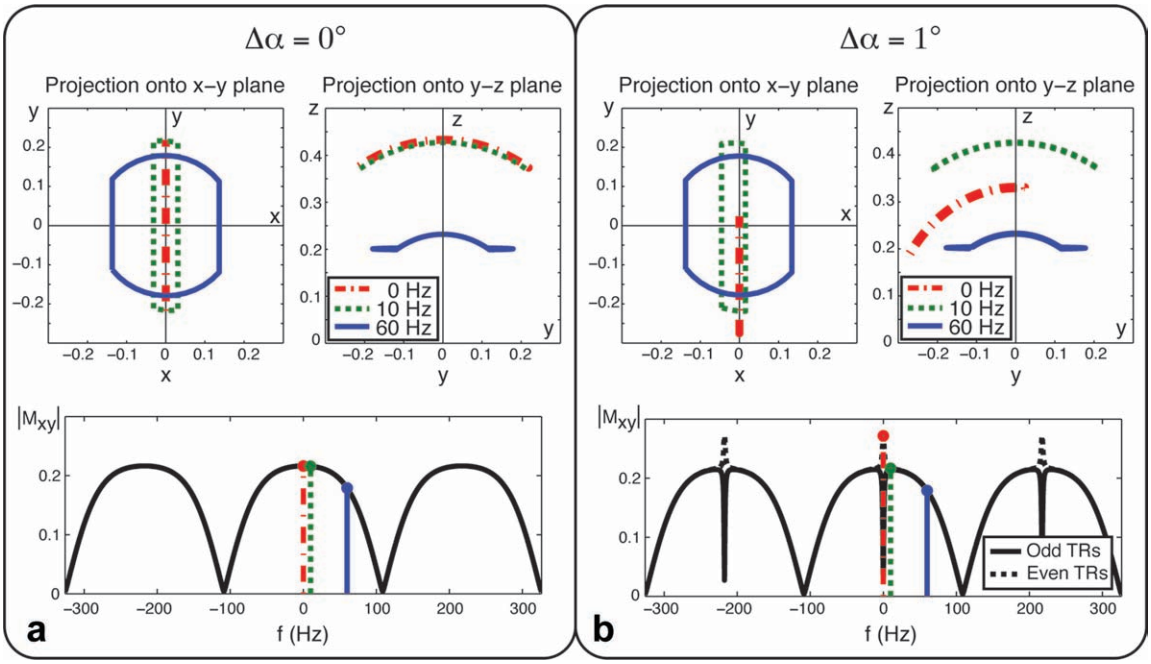

FIG. 5. The steady-state magnetization trajectories of the **(a)** bSSFP and **(b)** α-perturbed SSFP sequences were simulated for three off-resonant frequencies: 60 Hz, 10 Hz, and 0 Hz. a: For bSSFP, the *x*-*y* and *y*-*z* trajectories are symmetric. b: For α-perturbed SSFP, the steady-state trajectories at 60 Hz and 10 Hz rotate slightly to compensate for the net nutation angle of $\Delta\alpha = 1^\circ$ per period. This rotation is visible in the *x*-*y* projection as a slight shift of the profile in the $-x$ direction. For the 0-Hz trajectory, the magnetization is constrained to the *y*-*z* plane, and a very large rotation is required so that relaxation differences in odd and even TRs compensate for the additional nutation of $\Delta\alpha = 1^\circ$. This large rotation results in the sharp dips and spikes in the spectral profiles during odd and even TRs.

in the span of the corresponding eigenvectors. Figure 4b plots the resulting steady-state magnetization vectors during even and odd TRs. The steady-state magnetization vector of the unperturbed SSFP sequence is also plotted for comparison. The resulting change in direction of $\mathbf{M}_{ss}$ yields the narrow spikes and dips in the even and odd TRs of the α-perturbed spectral profile (Fig. 4c).

Magnetization Trajectory Analysis

In this section, we explain the central signal singularity phenomenon using a geometric approach that tracks the trajectory of the magnetization vector over time. For simplicity, we simulate and plot the trajectories of an α-perturbed SSFP sequence, but the technique is easily generalizable for analysis of ϕ-perturbed and TR-perturbed SSFP sequences as well as multi-TR sequences. Figure 5 plots the magnetization trajectories of a standard bSSFP sequence and an α-perturbed SSFP sequence with $\Delta\alpha = 1^\circ$. Trajectories are plotted for three different isochromats with off-resonant frequencies of 60 Hz, 10 Hz, and 0 Hz. Figure 5a shows projections of the bSSFP trajectory, which are symmetric about the coordinate axes. As the off-resonant frequency approaches 0 Hz, the amount of precession per TR decreases, and the magnetization becomes confined to the *y*-*z* plane, oscillating symmetrically about the *z*-axis due to the alternating $\pm\alpha^\circ$ excitations.

Figure 5b shows the trajectories of an α-perturbed sequence with $\Delta\alpha = 1^\circ$. The fundamental period of this sequence consists of an excitation with flip angle $(\alpha - \Delta\alpha/2)^\circ$ followed by an excitation with flip angle $-(\alpha + \Delta\alpha/2)^\circ$, yielding a net excitation of $-\Delta\alpha^\circ$ per period. Since the steady-state magnetization must return to the same magnitude and direction after each period, the magnetization trajectory must be asymmetric to compensate for the nonzero net excitation per period. At off-resonant frequencies that are far from 0 Hz (or integer multiples of 1/TR Hz), a significant amount of precession occurs between each excitation, and a small asymmetry of the magnetization trajectory is sufficient to compensate for the additional net excitation of $-\Delta\alpha^\circ$ per period. Compared with the symmetric trajectory of the unperturbed SSFP sequence, the transverse magnetization trajectory of the α-perturbed SSFP sequence is shifted by a small amount in the -*x* direction to account for the larger nutation angle of the even excitations. Thus, the resulting spectral profile of the α-perturbed sequence is very similar to that of the unperturbed SSFP sequence at off-resonant frequencies away from 0 Hz and integer multiples of 1/TR Hz.

At off-resonant frequencies of 0 Hz or integer multiples of 1/TR Hz, there is no net effective precession per TR, and the steady-state magnetization is constrained to the *y*-*z* plane. At these frequencies, the transverse magnetization trajectory of the perturbed sequence can no longer shift in the $\pm x$ direction to account for the nonzero net excitation per period. In the absence of relaxation, the magnetization would never reach steady state. Instead, it would experience a net rotation of $-\Delta\alpha^\circ$ each period and would circulate continuously in the *y*-*z* plane. In the presence of relaxation, the effects of transverse and longitudinal

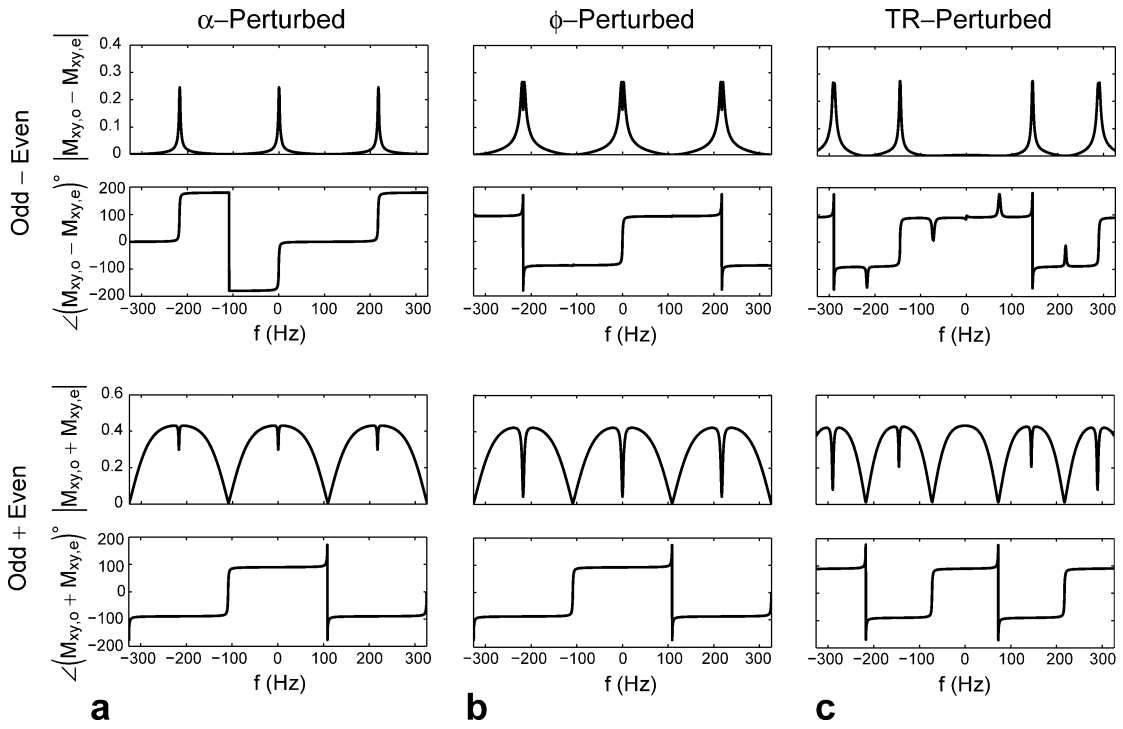

FIG. 6. The complex difference and complex sum of the odd-TR and even-TR spectral profiles were simulated for the **(a)** α-perturbed, **(b)** ϕ-perturbed, and **(c)** TR-perturbed SSFP sequences. The same sequence parameters were used as for the perturbed SSFP sequences in Fig. 2. At the critical frequencies, the transverse magnetization differs greatly between odd and even TRs, yielding the sharp peaks in the difference profiles and localized dips in the sum profiles. Away from the critical frequencies, the magnetization in even and odd TRs is relatively unchanged from the standard bSSFP sequence, yielding nulls in the difference profiles and bSSFP-like magnetization in the sum profiles. The phase profiles of the difference sequences contain 180° phase changes at the critical frequencies, yielding spectral profiles similar to those of low-flip-angle bSSFP. The phase profiles of the sum sequences contain 180° phase changes between each lobe of the magnitude profile, similar to the phase profiles of standard bSSFP.

relaxation during each TR are capable of offsetting the net rotation of $-\Delta\alpha^\circ$, and a non-zero steady-state solution can be achieved. The magnetization vector must be oriented closer to the transverse plane during even TRs and more longitudinally during odd TRs so that the subsequent relaxation differences during even and odd TRs will offset the flip-angle differences. If TR $\ll T_1, T_2$, the amount of relaxation per TR is small, and the steady-state magnetization trajectory must be highly asymmetric so that the relaxation differences will compensate for the differences in flip angle. The amount of asymmetry increases with the magnitude of the perturbation, since a larger relaxation difference is required to offset a greater difference in nutation angle. Likewise, longer T_1 and T_2 values result in more asymmetric steady-state solutions since there is less relaxation per TR.

Perturbed Differenced SSFP

By subtracting the even-TR and odd-TR spectral profiles, the resulting complex difference spectral profile contains nulls or very small magnitude away from the critical frequencies, where the even and odd profiles are very similar. Near the critical frequencies, the complex difference magnitude profile contains sharp peaks, where the even and odd profiles contain large, distinct deviations from the unperturbed profile. This technique, called Perturbed Differenced SSFP (pdSSFP), can be performed with α-perturbed, ϕ-perturbed, or TR-perturbed SSFP sequences. For clarity and consistence with other phase cycling schemes, the additional 180-degree phase due to the $(0, 180)^\circ$ phase schedule is removed from the even spectral profiles before subtraction.

Subtraction of even and odd spectral profiles of α-perturbed, ϕ-perturbed, and TR-perturbed sequences (Fig. 2a–c) yields the pdSSFP profiles (top row of Fig. 6a–c). The α-pdSSFP and ϕ-pdSSFP magnitude profiles each contain a periodic train of identical spikes, while the TR-pdSSFP magnitude profile contains spikes that increase in width away from 0 Hz. For each pdSSFP sequence, the spike width (FWHM) is a function of perturbation size ($\Delta\alpha$, $\Delta\phi$, or ΔTR), with larger perturbations resulting in wider spikes but less stopband attenuation around the signal nulls. Likewise, the amplitude of the spikes can be controlled by varying α, which can be optimized for a species with particular T_1 and T_2 values. The choice of TR controls the spacing of the spikes and nulls in the frequency domain, with spikes nominally spaced at intervals of 1/TR Hz. To shift the entire spectrum in the frequency domain, thereby aligning a spike or null with a particular frequency, the center frequency of the scanner can be varied. Alternatively, for α-pdSSFP or ϕ-pdSSFP, a linear phase cycling scheme can be applied. For TR-pdSSFP, however, the shape and width of the spectral spikes vary with

off-resonant frequency location, as described below, and only variation of the center frequency will preserve the profile shape.

There are subtle differences between the α-pdSSFP, ϕ-pdSSFP, and TR-pdSSFP profiles that should be noted. The spectral spikes in the α-pdSSFP and ϕ-pdSSFP profiles are the same across all critical frequencies, while the spikes in the TR-pdSSFP profile have varying shapes and widths. The widths of the central signal singularity increase at higher critical frequencies, as can be seen in both the difference and sum profiles in Fig. 6c. The shape variations are most apparent in the sum profile, visible as deeper notches at higher critical frequencies (Fig. 6c). Due to the finite resolution of the plots in Fig. 6c, the shape variations are not visible in the difference profile. The α-pdSSFP and ϕ-pdSSFP spectral spikes result from steady-state magnetization deviations that are induced to offset the flip-angle or phase differences between even and odd excitations, and these differences are independent of off-resonant frequency. On the other hand, the TR-pdSSFP spikes are caused by frequency-dependent precession differences between even and odd TRs. At the $f = 0$ Hz critical frequency, there is zero precession in both even and odd TRs, which results in no perturbation of the steady-state magnetization and thus no spike in the TR-pdSSFP profile. At the next critical frequency, $f = \pm 1/\mathrm{TR}$ Hz, there is a precession difference of $2\pi(\Delta\mathrm{TR}/\mathrm{TR})$ between even and odd TRs, which yields spikes in the TR-pdSSFP profile at the corresponding off-resonant frequencies. At the next critical frequency away from 0 Hz, $f = \pm 2/\mathrm{TR}$ Hz, the precession difference is doubled to $4\pi(\Delta\mathrm{TR}/\mathrm{TR})$, which results in larger perturbations of the steady-state magnetization and subsequently, wider spikes in the TR-pdSSFP profile.

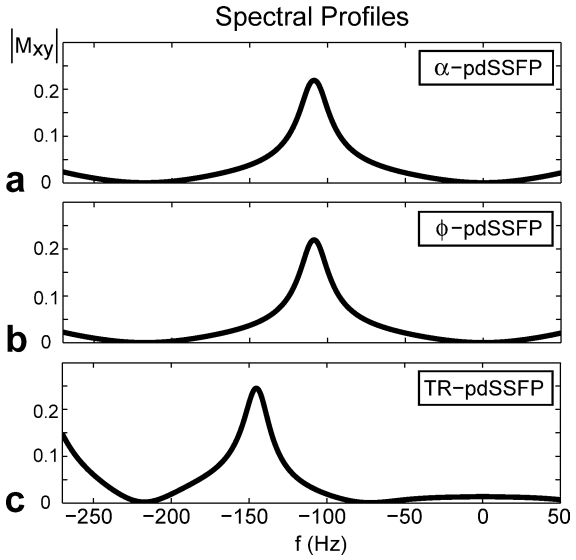

FIG. 7. The spectral profiles were simulated for the **(a)** α-pdSSFP, **(b)** ϕ-pdSSFP, and **(c)** TR-pdSSFP sequences using the T_1 and T_2 values of the agar gel phantom containing SPIO nanoparticles (T_1/T_2 = 265/30 ms) and (a) $\alpha = 40°$, $\Delta\alpha = 6°$, TR = 4.6 ms, and $\phi = (0, 0)°$, (b) $\alpha = 40°$, $\Delta\phi = 9°$, TR = 4.6 ms, and $\phi = (0, 0)°$, and (c) $\alpha = 30°$, ΔTR = 0.55 ms, TR = 6.9 ms, and $\phi = (0, 180)°$. A longer TR of 6.9 ms and a $(0, 180)°$ phase cycling schedule were used for the TR-pdSSFP sequence since it does not have signal perturbations at the 0-Hz critical frequency. The α-pdSSFP and ϕ-pdSSFP profiles are very similar, having nulls on the water and fat resonances at 1.5 T and a wide, high-amplitude peak centered midway between the two resonances. The TR-pdSSFP profile has a spectral peak that is centered closer to the fat resonance, yielding reduced signal suppression in the fat stopband. The profile has a wide region of signal suppression throughout the water stopband.

Perturbed Summed SSFP

Analogous to pdSSFP, the even and odd profiles can instead be summed (bottom row of Fig. 6). Of particular interest is the TR-perturbed summed profile (Fig. 6c), which contains a central lobe that is free of perturbations. Since this central lobe is very similar to that of the bSSFP profile, the TR-perturbed summed sequence can be used to acquire images with contrast similar to bSSFP, while the differenced sequence can be used to yield positive contrast from highly off-resonant regions in the object.

METHODS

In the following sections, we demonstrate the features of the pdSSFP sequences via an application to positive-contrast imaging, in which field perturbations near iron-containing contrast agents yield regions of hyperintense signal. With the appropriate choices of flip angle, $\Delta\alpha/\Delta\phi/\Delta$TR, and phase cycling, the pdSSFP sequences are well-suited for positive-contrast imaging applications. In this section, we select pdSSFP sequence parameters, use simulations to analyze and compare the resulting spectral profiles, and describe the phantom experiments performed to demonstrate the application of the pdSSFP sequences to positive-contrast imaging.

Simulations

For each pdSSFP sequence, the phase cycling and TR can be chosen to align signal nulls with the water and fat resonant frequencies, yielding robust background suppression for positive-contrast imaging applications. For α-pdSSFP and ϕ-pdSSFP sequences, a TR of 4.6 ms and a $(0, 0)°$ phase schedule align signal nulls with water and fat resonances at 1.5 T, with a signal peak located midway between at $f = -1/(2\,\mathrm{TR})$ Hz. Because the TR-pdSSFP sequence does not have a spectral peak at the 0-Hz critical frequency (Fig. 6c), a longer TR of 6.9 ms and a $(0, 180)°$ phase schedule are required to place a signal null on the fat resonance as well as position a signal peak between the water and fat resonances. These parameter choices also result in a broad stopband around the water resonance.

The spectral profiles of each pdSSFP sequence are plotted in Fig. 7 using these values of TR and phase cycling schemes. The following flip angles and perturbation sizes were chosen for each sequence to yield a good trade-off between contrast-to-noise ratio (CNR) and fat and water background suppression: $\alpha = 40°$ and $\Delta\alpha = 6°$ (α-pdSSFP), $\alpha = 40°$ and $\Delta\phi = 9°$ (ϕ-pdSSFP), and $\alpha = 30°$ and ΔTR = 0.55 ms (TR-pdSSFP). The α-pdSSFP and ϕ-pdSSFP profiles have nulls at both water and fat resonances, and they have broad, high-amplitude peaks that yield high CNR.

Table 1
Sequence Parameters

Sequence	α (°)	ϕ (°)	TR (ms)	TE (ms)	TR_{odd}/TR_{even} (ms)	Perturbation
GRE	30	–	21	6	–	–
α-pdSSFP	40	(0, 0)	4.6	2.3	–	$\Delta\alpha = 6°$
ϕ-pdSSFP	40	(0, 0)	4.6	2.3	–	$\Delta\phi = 9°$
TR-pdSSFP	30	(0, 180)	6.9	3.3/3.6	6.6/7.2	$\Delta TR = 0.55$ ms

The TR-pdSSFP sequence has a signal null at the fat resonant frequency, and it has a broad but nonzero stopband around the water resonant frequency. The signal peak is located at a higher off-resonant frequency than α-pdSSFP and ϕ-pdSSFP, which could reduce unwanted positive contrast around air-tissue interfaces and other regions with moderate magnetic susceptibility differences. Since the peak is close to the fat resonance, however, the TR-pdSSFP sequence has poorer fat background suppression than α-pdSSFP or ϕ-pdSSFP.

Phantom Experiments

The spectral profiles of the three pdSSFP sequences were verified by scanning a uniform spherical phantom ($T_1/T_2 = 370/300$ ms). A linear gradient shim was applied along the right/left direction to create a spatially-varying off-resonant frequency across the phantom. The sequence parameters for the α-pdSSFP, ϕ-pdSSFP, and TR-pdSSFP sequences are summarized in Table 1. For each pdSSFP sequence, two interleaved 3D acquisitions were obtained during even and odd TRs using a 24-cm FOV, $0.94 \times 0.94 \times 3$ mm^3 resolution, and $256 \times 256 \times 60$ encoding matrix. The resulting even and odd complex images were subtracted to yield the pdSSFP spectral images. Bloch simulations were performed to compare the theoretical profiles with cross-sectional profiles from each of the measured spectral images.

An agar gel phantom ($T_1/T_2 = 265/30$ ms) containing SPIO nanoparticles was constructed to demonstrate and compare the levels of positive contrast and background suppression of the pdSSFP sequences. A cylindrical gel phantom composed of 4% agar by weight and 8 mM $NiCl_2$ was prepared. The phantom contained four cylindrical wells that were filled with agar solutions doped with 100, 200, 400, and 800 μg/mL concentrations of SPIO fluidMAG-D nanoparticles (Chemicell, Berlin, Germany).

The agar gel SPIO phantom and an oil phantom were simultaneously imaged using a birdcage head coil on a 1.5-T GE Signa scanner (GE Healthcare, Waukesha, WI) with gradients capable of 40 mT/m amplitude and 150 mT/m/ms slew rate. Three-dimensional gradient-recalled echo (GRE) and pdSSFP images were collected with the following common set of parameters: 16-cm FOV, $0.83 \times 0.83 \times 1$ mm^3 resolution, and $192 \times 192 \times 60$ encoding matrix. Readout bandwidths of ± 31.25 kHz (GRE) and ± 62.5 kHz (pdSSFP) were used. The sequence parameters are summarized in Table 1. To normalize the total scan time across all positive-contrast sequences, α-pdSSFP and ϕ-pdSSFP acquisitions were averaged 3 times and the TR-pdSSFP acquisition was averaged 2 times to yield a total scan time of 5 min 45 s for all positive-contrast sequences.

RESULTS

The spherical phantom spectral images acquired with the α-pdSSFP, ϕ-pdSSFP, and TR-pdSSFP sequences are shown in Fig. 8. Measured cross-sectional profiles from each image agree well with simulated spectral profiles. The sum of even and odd acquisitions from the TR-perturbed sequence is shown in the bottom row of Fig. 8. The spectral profile contains a central lobe that is free of perturbations, which can be used to acquire images with contrast similar to bSSFP.

The SPIO and oil phantom images acquired with the GRE and pdSSFP sequences are shown in Fig. 9. The GRE

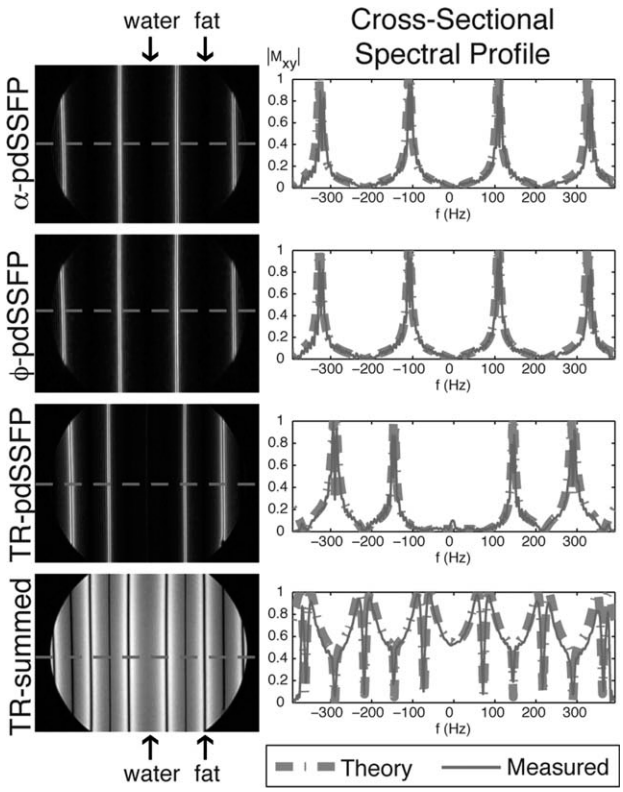

FIG. 8. A homogeneous spherical phantom ($T_1/T_2 = 370/300$ ms) was scanned using a linear field gradient in the right/left direction to induce a spatially-varying precession frequency. The same sequence parameters were used as in Fig. 7. Cross-sectional profiles are plotted in the right column along with the simulated spectral profiles (dot-dash line). The measured pdSSFP profiles agree very well with theory, having signal nulls located at the water and fat resonances and sharp peaks in between. The measured TR-summed profile also agrees well with theory, having a central lobe that is essentially identical to that of the standard bSSFP profile. [Color figure can be viewed in the online issue, which is available at wileyonlinelibrary.com.]

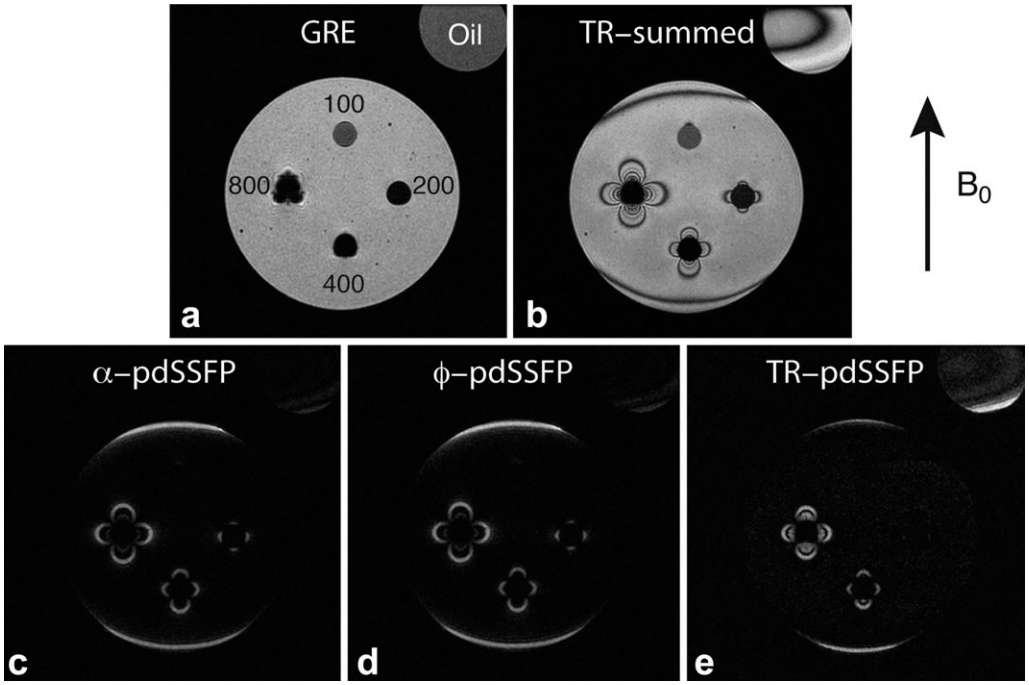

FIG. 9. An agar gel phantom ($T_1/T_2 = 265/30$ ms) containing four regions doped with SPIO nanoparticles was scanned at 1.5 T with **(a)** GRE, **(b)** TR-summed, **(c)** α-pdSSFP, **(d)** ϕ-pdSSFP, and **(e)** TR-pdSSFP pulse sequences. The SPIO concentrations are marked on the GRE image in μg/mL. Additionally, an oil phantom was simultaneously imaged to assess the fat suppression of the pdSSFP sequences. The TR-summed sequence produces an image with contrast similar to bSSFP. The characteristic bSSFP banding artifacts, due to field inhomogeneities, are visible at the top and bottom of the agar gel phantom and within the oil phantom. The α-pdSSFP and ϕ-pdSSFP sequences produce very similar positive-contrast images containing very good water and fat background suppression as well as regions of positive contrast surrounding the 200, 400, and 800 μg/mL SPIO wells. The TR-pdSSFP sequence results in slightly poorer fat suppression, and the areas of positive contrast are located closer to the SPIO regions and are only visible around the 400 and 800 μg/mL SPIO wells. The bright regions at the top and bottom of the agar gel phantom in (c)–(e) are due to susceptibility shifts from the agar-air interface, which is perpendicular to B_0 in these locations.

image contains hypointense signal from the four regions doped with SPIO nanoparticles, and each region is labeled with the corresponding nanoparticle concentration. The α-pdSSFP and ϕ-pdSSFP images both show good suppression of water and fat background signal, with bright regions of positive contrast visible around the 200, 400, and 800 μg/mL SPIO wells. Although the TR-pdSSFP sequence lacks a signal null on the water resonance, the suppression of water background signal in Fig. 9e is not significantly inferior to that of α-pdSSFP or ϕ-pdSSFP. The fat suppression of the TR-pdSSFP sequence is poorer because the spectral profile has a narrower null on the fat resonance, making the fat suppression more susceptible to field inhomogeneities. The regions of positive contrast are only visible around the 400 and 800 μg/mL SPIO wells, which can be attributed to the fact that the first off-resonant peak of the TR-pdSSFP profile is centered at a higher off-resonant frequency than α-pdSSFP and ϕ-pdSSFP. The TR-perturbed summed image has contrast similar to a standard bSSFP sequence. Note that the thin bands of positive contrast at the bottom and top of the agar gel phantom in Fig. 9c–e are due to the susceptibility differences caused by the phantom-air interface. Likewise, the dark bands visible in similar locations in Fig. 9b are bSSFP-like banding artifacts caused by these susceptibility differences. The B_0 field was perpendicular to these signal bands, oriented vertically in these images.

DISCUSSION

We have presented algebraic and geometric explanations of the central signal singularity phenomenon, which were used to show that the critical frequencies are located at singularities in the steady-state signal equation. At these frequencies, small perturbations of the SSFP parameters can yield very large deviations in the spectral profile. If sequence parameters are symmetric, as in the case of bSSFP, the system matrix **R** is typically symmetric at these critical frequencies, having three real eigenvalues, with one dominant eigenvalue that is closest to 1. For these sequences, the steady-state magnetization continues to track the dominant eigenvector at these critical frequencies, resulting in a smooth spectral profile. When parameter perturbations are introduced, **R** is no longer symmetric at these critical frequencies and typically contains two complex eigenvalues that are dominant. The steady-state magnetization no longer tracks the real eigenvector at these frequencies, resulting in a sharp deviation in the spectral profile.

Though we illustrated the eigendecomposition and geometric analysis techniques using a specific α-perturbed

SSFP sequence, these methods can be used in the analysis and design of any balanced steady-state sequence. By finding the critical frequencies of a steady-state sequence, the potential locations of spectral perturbations can be isolated. The sequence parameters (α, ϕ, TR) can then be modified to enhance or reduce the spectral perturbations at these critical frequencies, depending on the desired application.

Using the theory and explanation of the central signal singularity, we developed the pdSSFP pulse sequences and demonstrated their application to positive-contrast imaging. As shown in Fig. 7, the α- and ϕ-pdSSFP sequences have nearly identical spectral profiles, containing high-amplitude spectral peaks with signal nulls on the water and fat resonances. The effects of these features are visible in Fig. 9c, d, which have good water and fat background suppression and positive contrast surrounding the 200, 400, and 800 μg/mL SPIO regions. In practice, the ϕ-pdSSFP sequence could be a preferred approach since the RF phase can typically be controlled more precisely than flip angle on MR scanners. However, both sequences are robust to B_1 inhomogeneities since they depend only on the relative flip-angle or phase difference between even and odd excitations.

The spectral peak of the TR-pdSSFP sequence is centered closer to the fat resonance, which results in reduced fat suppression as well as reduced positive contrast from smaller concentrations of SPIO nanoparticles that induce smaller field inhomogeneities. The TR-pdSSFP sequence also lacks a signal null at the water resonance, but this deficiency did not lead to significantly inferior water suppression in Fig. 9e. In fact, the broad stopband around the water resonance could yield more robust water background suppression in the presence of field inhomogeneities. A unique feature of the TR-perturbed sequence is the ability to simultaneously generate positive-contrast images (by subtracting the even and odd echoes) and bSSFP-like images (by summing the even and odd echoes). The spectral profile of the TR-summed sequence contains a central lobe that is very similar to bSSFP, however, the longer TR of 6.9 ms and the central signal singularities at higher critical frequencies will lead to additional banding compared to a standard bSSFP acquisition (Fig. 9b).

Similar to other steady-state techniques, the pdSSFP sequences have the advantages of high SNR efficiency and the potential for high-resolution, fast 3D imaging. Due to the interleaved acquisition technique, we expect the pdSSFP sequences to be more immune to motion effects than sequential subtraction techniques. Similar to other steady-state positive-contrast sequences, a drawback of pdSSFP is that positive contrast is generated via off-resonant excitation. This requires sufficiently high concentrations of SPIO nanoparticles to yield a frequency offset that will generate positive contrast. Furthermore, regions of considerable field inhomogeneity or abrupt changes in susceptibility can result in unwanted positive contrast, which can reduce the specificity of the sequences to SPIO-labeled regions. The pdSSFP sequences have higher specific absorption rates (SAR) than low-flip-angle positive-contrast techniques (19,22), but the flip angles are not excessively large, resulting in SAR levels that are comparable to typical bSSFP sequences.

We demonstrated an application of the central signal singularity phenomenon for positive-contrast imaging of SPIO nanoparticles. This particular application was chosen to demonstrate the features and capabilities of this imaging technique, but by no means is this the only application of the central signal singularity phenomenon. Other potential applications of the pdSSFP sequence include those that require spectrally-selective acquisition of a narrow band of off-resonant frequencies, such as MR spectroscopy, as well as off-resonance angiography (26), transition-band SSFP fMRI (27,28), and other applications similar to those of low-flip-angle bSSFP.

CONCLUSION

The central signal singularity phenomenon has been analyzed via a linear systems eigendecomposition technique and a geometric magnetization trajectory technique. The large spectral profile deviations resulting from perturbations of bSSFP parameters were shown to coincide with singularities in the steady-state signal equation. The phenomenon was used to create a perturbed differenced SSFP sequence, and this sequence was demonstrated for positive-contrast-imaging applications. Simulations, spectral measurements, and agar gel SPIO phantom scans were carried out for α-pdSSFP, ϕ-pdSSFP, and TR-pdSSFP sequences. The pdSSFP sequences achieve simultaneous suppression of water and fat background signal as well as positive contrast from off-resonant spins. Additionally, the TR-pdSSFP sequence is capable of producing both positive-contrast images and anatomic images by differencing or summing the even and odd echoes.

REFERENCES

1. Carr HY. Steady-state free precession in nuclear magnetic resonance. Phys Rev 1958; 112:1693–1701.
2. Oppelt A, Graumann R, Barfuss H, Fischer H, Hartl W, Shajor W. FISP—a new fast MRI sequence. Electromedica 1986;54:15–18.
3. Zur Y, Stokar S, Bendel P. An analysis of fast imaging sequences with steady-state transverse magnetization refocusing. Magn Reson Med 1988;6:175–193.
4. Zur Y, Wood ML, Neuringer LJ. Motion-insensitive, steady-state free precession imaging. Magn Reson Med 1990;16:444–459.
5. Bangerter NK, Hargreaves BA, Vasanawala SS, Pauly JM, Gold GE, Nishimura DG. Analysis of multiple-acquisition SSFP. Magn Reson Med 2004;51:1038–1047.
6. Vasanawala SS, Pauly JM, Nishimura DG. Fluctuating equilibrium MRI. Magn Reson Med 1999;42:876–883.
7. Vasanawala SS, Pauly JM, Nishimura DG. Linear combination steady-state free precession MRI. Magn Reson Med 2000;43:82–90.
8. Overall WR, Nishimura DG, Hu BS. Steady-state sequence synthesis and its application to efficient fat-suppressed imaging. Magn Reson Med 2003;50:550–559.
9. Leupold J, Hennig J, Scheffler K. Alternating repetition time balanced steady state free precession. Magn Reson Med 2006;55:557–565.
10. Absil J, Denolin V, Metens T. Fat attenuation using a dual steady-state balanced-SSFP sequence with periodically variable flip angles. Magn Reson Med 2006;55:343–351.
11. Bieri O, Maderwald S, Ladd ME, Scheffler K. Balanced alternating steady-state elastography. Magn Reson Med 2006;55:233–241.
12. Scheffler K, Maderwald S, Ladd ME, Bieri O. Oscillating steady states. Magn Reson Med 2006;55:598–603.
13. Nayak KS, Lee HL, Hargreaves BA, Hu BS. Wideband SSFP: alternating repetition time balanced steady state free precession with increased band spacing. Magn Reson Med 2007;58:931–938.
14. Cukur T, Nishimura DG. Fat-water separation with alternating repetition time balanced SSFP. Magn Reson Med 2008;60:479–484.

15. Cukur T, Nishimura DG. Multiple repetition time balanced steady-state free precession imaging. Magn Reson Med 2009;62:193–204.
16. Ingle RR, Cukur T, Nishimura DG. Spectral profile design for multiple repetition time balanced SSFP. In: Proceedings of the 18th Annual Meeting of ISMRM, Stockholm, Sweden, 2010. p 75.
17. Overall WR, Conolly SM, Nishimura DG, Hu BS. Oscillating dual-equilibrium steady-state angiography. Magn Reson Med 2002;47: 513–522.
18. Cunningham CH, Arai T, Yang PC, McConnell MV, Pauly JM, Conolly SM. Positive contrast magnetic resonance imaging of cells labeled with magnetic nanoparticles. Magn Reson Med 2005;53: 999–1005.
19. Dharmakumar R, Koktzoglou I, Li D. Generating positive contrast from off-resonant spins with steady-state free precession magnetic resonance imaging: theory and proof-of-principle experiments. Phys Med Biol 2006;51:4201–4215.
20. Stuber M, Gilson WD, Schär M, Kedziorek DA, Hofmann LV, Shah S, Vonken EJ, Bulte JW, Kraitchman DL. Positive contrast visualization of iron oxide-labeled stem cells using inversion-recovery with ON-resonant water suppression (IRON). Magn Reson Med 2007;58: 1072–1077.
21. Overall WR, Pauly JM. Positive-contrast imaging of microscopic paramagnetic particles using field-encoded fluctuating-equilibrium SSFP. In: Proceedings of the 16th Annual Meeting of ISMRM, Toronto, Canada, 2008. p 1445.
22. Cukur T, Yamada M, Overall WR, Yang P, Nishimura DG. Positive contrast with alternating repetition time SSFP (PARTS): a fast imaging technique for SPIO-labeled cells. Magn Reson Med 2010;63:427–437.
23. Jaynes ET. Matrix treatment of nuclear induction. Phys Rev 1955; 98:1099–1105.
24. Hargreaves BA, Vasanawala SS, Pauly JM, Nishimura DG. Characterization and reduction of the transient response in steady-state MR imaging. Magn Reson Med 2001;46:149–158.
25. Schmitt P, Griswold MA, Gulani V, Haase A, Flentje M, Jakob PM. A simple geometrical description of the TrueFISP ideal transient and steady-state signal. Magn Reson Med 2006;55:177–186.
26. Edelman RR, Storey P, Dunkle E, Li W, Carrillo A, Vu A, Carroll TJ. Gadolinium-enhanced off-resonance contrast angiography. Magn Reson Med 2007;57:475–484.
27. Scheffler K, Seifritz E, Bilecen D, Venkatesan R, Hennig J, Deimling M, Haacke EM. Detection of BOLD changes by means of a frequency-sensitive trueFISP technique: preliminary results. NMR Biomed 2001;14:490–496.
28. Miller KL, Hargreaves BA, Lee J, Ress D, deCharms RC, Pauly JM. Functional brain imaging using a blood oxygenation sensitive steady state. Magn Reson Med 2003;50:675–683.